Stability Analysis and Comprehensive Design of Grid-tied Inverter with Active Damped *LCL* Filter

Jun-ichi Itoh
Dept. Science of Technology Innovation
Nagaoka University of Technology
Nagaoka, Japan
itoh@vos.nagaokaut.ac.jp

Tetsunori Kinoshita
Dept. Electrical, Electronics, and Information Engineering
Nagaoka University of Technology
Nagaoka, Japan
kinoshita_t@stn.nagaokaut.ac.jp

Akio Toba
Fuji Electric Co., Ltd.
Tokyo, Japan
toba-akio@fujielectric.com

Satoru Fujita
Fuji Electric Co., Ltd.
Tokyo, Japan
fujita-satoru@fujielectric.com

***Abstract*— This paper proposes a comprehensive design strategy for an *LCL* filter and controller parameters of an active damped *LCL* filter which has low inverter-side inductance in a grid-tied inverter. Design methods of a current controller and an active damping gain become more challenging because grid impedance affects the stability when the inverter-side inductance is low. First, a maximum damping gain range is derived to achieve a virtual positive damping resistor with cutoff frequency of high-pass-filter (HPF) and the *LCL* resonance frequency. Next, the practical implementation solutions are discussed based on the proposed design procedure. The detailed design strategy is exhibited with the design procedure and the design example. The validity of the theoretical analysis is demonstrated by a 1-kW prototype with or without the designed active damping. The grid current THD below 1.2% is maintained over the grid impedance range from 0% to 10%.**

Keywords— Active damping, LCL filter design, Grid current feedback control

I. Introduction

An output filters in single-phase grid-tied inverters are required to suppress current harmonics and meet the grid current harmonics standards such as IEEE 1547 [1] with small filter parameters. An *LCL* filter is widely used to obtain an effect of the switching harmonic attenuation with the lower inductance compared to the *L* filters. However, the current control loop becomes unstable due to the *LCL* filter resonance even if the proportional gain is small in the grid-tied inverter with the *LCL* filters [2]-[5].

On the other hand, the computation delay and the PWM delay due to zero-order-hold (ZOH) occur when digital control is applied, i.e. DSP and FPGA. Generally, in the grid-tied system with the *LCL* filter, the grid current feedback control system is well-known unstable when the resonance frequency is less than quarter of sampling frequency f_{samp} [6]-[12]. According to [13], in the grid current feedback control system, an appropriate delay is required for stable operation. However, the excessive delay causes worse control performance, i.e. reducing control bandwidth. If the resonance frequency is less than $f_{samp}/4$, the current control system requires some attenuation, i.e. the passive damping or the active damping.

Therefore, the active damping methods based on concepts of a virtual resistor has been proposed in order to suppress the *LCL* resonance and avoid the power loss of the passive resistor [14]-[16]. In general, an active damping method uses the filter capacitor current feedback through a proportional gain or a high-pass filter (HPF). In these active damping methods, a virtual resistor or a virtual *RC* damper are respectively provided in parallel with the filter capacitor. However, these damping methods is not effective when the virtual resistor seem to a negative resistance depending on the ratio of the *LCL* filter resonance frequency to the sampling frequency under considering the digital sampling and computational delays [10]. The current control block diagram contains the virtual negative damping resistor by the open-loop [14], [15]. Note that the step response includes the unfavorable inverse response due to the virtual negative damping resistor. The conventional design strategy focuses on the design of the *LCL* filter parameters and the parameters of the active damping controller, which are the insufficient design strategy for minimized the *LCL* filter for high power density. In particular, the current controller and the active damping gain designs considering the resonance in the *LCL* filter become more challenging due to a wide variation range of the grid impedance when the inverter-side inductor is low-inductance. Nevertheless, the design strategy of a filter, the current controller, and active damping gain considered the *LCL* filter with low inductance has not been reported.

This paper proposes a comprehensive design strategy for the *LCL* filter, active damping controller parameters, and current controller parameters of the active damped *LCL* filter system with the low inverter-side inductance in a grid-tied inverter. The new contribution of this paper is that the stability range is provided by the diagram easily in unrelated to the rating of the output power and voltage. The practical implementation solutions are discussed based on the proposed design procedure. The detailed design strategy is exhibited with the design procedure and the design example. The validity of the theoretical analysis is demonstrated by a 1-kW prototype with or without active damping.

This paper is organized as follows; first, the issue of the proportional active damping is explained, and the HPF active damping method is employed to extend the range of the positive virtual resistance. In addition, the practical implementation solutions are discussed based on the proposed design procedure in Section II. Second, the design procedure of the *LCL* filter, the active damping controller parameters, and the current controller parameters are presented, and the detailed design strategy is exhibited in Section III. Third, in Section IV, the design example is introduced for the experiments. Fourth, the experiment results are provided in order to validate the theoretical analysis in Section V. Finally, Section VI concludes this paper.

II. Capacitor Current Feedback Acttive Damping

Fig. 1 indicates the circuit configuration of the single-phase grid-tied inverter with an *LCL* filter. In this paper, a single-phase H-bridge two-level inverter is applied due to its simplicity. In this paper, the grid current, capacitor current, and capacitor voltage are detected for the current control, active damping, and phase-locked-loop.

A. Negative resistance issue of active damping

Fig. 2 shows the block diagram of the grid current feedback control system and the equivalent circuit. As shown in Fig. 2, by employing the active damping, the virtual impedance $Z_{AD}(j\omega)$ is connected in parallel with the filter capacitor. The virtual impedance is constructed with the virtual resistance R_{AD} and the virtual reactance X_{AD}. The virtual resistance can be the negative value due to the change of the resonance frequency by considering the delay time [15]. Thus, the virtual resistance with the HPF-active-damping is expressed as follows;

$$R_{AD}(j\omega)=\frac{L}{K_t C_f}\left(\cos\omega T_{samp}+\frac{\omega_{hpf}}{\omega}\sin\omega T_{samp}\right) \tag{1,}$$

where L is the inverter-side inductance, C_f is the filter capacitance, T_{samp} is the sampling period, K_t is the active damping gain, and f_{hpf} (= $\omega_{hpf}/2\pi$) is the cutoff frequency of HPF. According to (1), the resonance frequency range of the positive resistance is less than $f_{samp}/4$ when $f_{hpf}=0$, i.e. the proportional active damping is employed [17]. On the other hand, the resonance frequency range of the negative resistance is avoided by increasing the cutoff frequency of HPF. However, if the cutoff frequency of HPF is set to higher than the Nyquist frequency, the effect of observation noise increases. Thus, the resonance frequency range of the positive resistance is less than $0.39f_{samp}$ when the cutoff frequency of HPF in (1) is set to $0.5f_{samp}$.

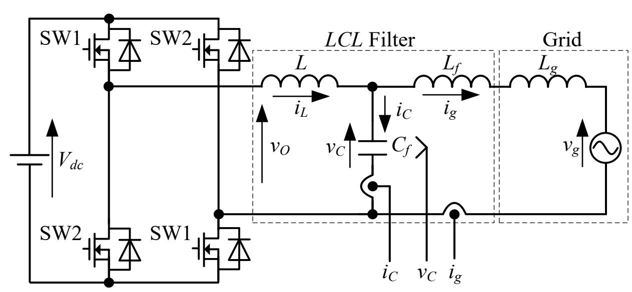

Fig. 1. Single-phase grid-tied inverter with *LCL* filter.

B. Discretized model

The modified pulse transfer functions of the inverter-output-voltage-to-grid-current $G_{vo\to ig}[z,m]$ and the inverter-output-voltage-to-filter-capacitor-current $G_{vo\to ic}[z,m]$ from Fig. 2 are expressed as follows to evaluate the current control stability, respectively

$$G_{v_O\to i_g}[z,m]=\frac{i_g}{v_O}=\frac{z-1}{z}\frac{1}{L+L_f+L_g}\cdot \left\{\frac{T_{samp}\left[m(z-1)+1\right]}{(z-1)^2}-\frac{z\sin m\omega_r T_{samp}+\sin(1-m)\omega_r T_{samp}}{\omega_r\left(z^2-2z\cos\omega_r T_{samp}+1\right)}\right\} \tag{2}$$

$$G_{v_O\to i_C}[z,m]=\frac{i_C}{v_O}=\frac{z-1}{z}\frac{1}{L\omega_r}\frac{z\sin m\omega_r T_{samp}+\sin(1-m)\omega_r T_{samp}}{z^2-2z\cos\omega_r T_{samp}+1} \tag{3,}$$

$$f_r=\frac{\omega_r}{2\pi}=\frac{1}{2\pi}\sqrt{\frac{L+L_f+L_g}{L\left(L_f+L_g\right)C_f}} \tag{4,}$$

where f_r is the resonance frequency of the *LCL* filter, L_f is the grid-side filter inductance, and L_g is the gird inductance. Note that m is 1-λ, and λ is the variable that depends on the duty update timing [6], [7]. λ is 0.5 when sampling at the top of the carrier and updating at the bottom of the carrier. In this paper, λ is discussed at 0.5. HPF for the virtual *RC* damper is discretized by Tustin transformation, which is expressed by

$$G_{AD}[z]=\frac{2K_t(z-1)}{\left(2+\omega_{hpf}T_{samp}\right)z+\omega_{hpf}T_{samp}-2} \tag{5.}$$

C. Inner loop stable region

Fig. 3 shows the block diagram of the discretized grid current feedback control system with the active damping. As shown in Fig. 3, the two types loop are introduced: the outer loop is the grid current feedback control loop, and the inner loop is the filter capacitor current feedback loop for the active damping. The stability of the inner loop depends on (3) and (5). The closed-loop pulse transfer function of the inner loop is expressed as

$$G_{closed\_inner}[z]=\frac{1}{1+G_{AD}[z]G_{v_O\to i_C}[z,m]} \tag{6.}$$

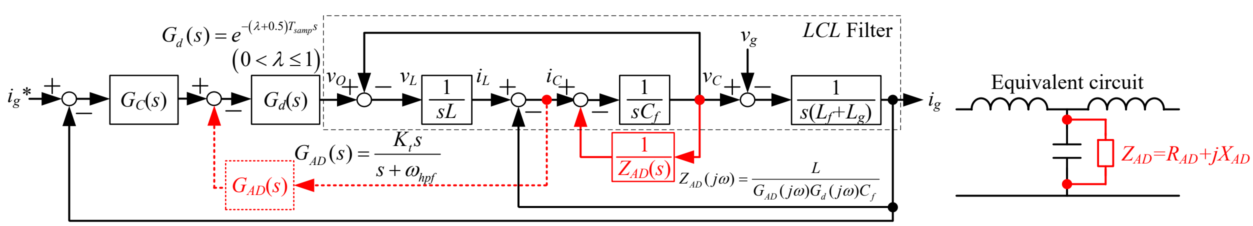

(a) Grid current feedback control system with active damping. (b) Equivalent circuit.

Fig. 2. Block diagram of grid current feedback control system and equivalent circuit. Active damping is equivalent to virtual impedance Z_{AD} connected in parallel with filter capacitor C_f.

Identify applicable funding agency here. If none, delete this text box.

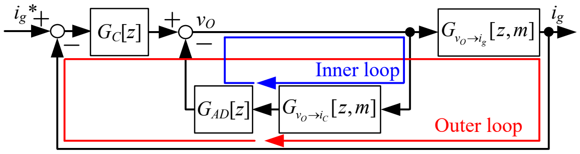

Fig. 3. Discretized grid current feedback system with active damping.

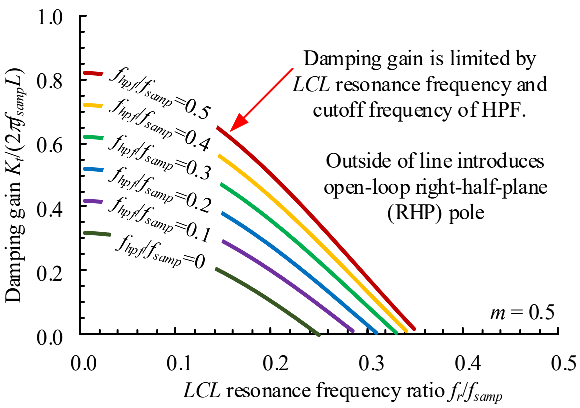

Fig. 4. Maximum active damping gain range to achieve inner loop stability with cutoff frequency of HPF and LCL resonance frequency.

The stability criterion of the closed-loop pulse transfer function in the z-dominant is determined from the roots of the denominator characteristic equation. The system is stable when all poles are in the unit circle. Note that the poles of (6) have a complex conjugate pole, and the condition for arranging the poles on the unit circle is expressed by

$$K_t = \frac{2+\omega_{hpf}T_{samp}}{2}\frac{L\omega_r}{\sin(1-m)\omega_r T_{samp}}\cdot \frac{(2\cos\omega_r T_{samp}-h)\sin(1-m)\omega_r T_{samp}+\sin m\omega_r T_{samp}}{\sin m\omega_r T_{samp}+(2-h)\sin(1-m)\omega_r T_{samp}} \tag{7}$$

where $h = (2-\omega_{hpf}T_{samp}) / (2+\omega_{hpf}T_{samp})$.

Fig. 4 depicts the maximum active damping gain range to achieve the inner loop stability for the cutoff frequency of HPF and the LCL resonance frequency. As shown in Fig. 4, the high cutoff frequency of HPF is required for the active damping under the high LCL resonance frequency to achieve the inner loop stability with the same damping gain, which is consistent with (1). Fig. 4 and (7) show the relationship of each parameter to achieve the stable inner loop. However, (7) shows only the stability limit. The next step is to evaluate based on the stability margin, i.e. the gain margin and the phase margin.

Fig. 5 depicts the definition of gain and phase margins of the inner loop. As shown in Fig. 5, a gain margin GM and two phase margins PM_1, PM_2 are defined. The gain margin GM and the phase margin PM_2 of the inner loop are improved by decreasing the LCL resonance frequency, whereas the phase margin PM_1 of the inner loop worse due to decreasing the LCL resonance frequency. Note that the phase margin PM_2 decreases due to the unknown delay of the real system, i.e. detection delay. Generally, the gain margin and phase margin are recommended to be not less than 3dB and 30 degrees, respectively [16]. If the LCL resonance frequency is $f_{samp}/3$ or more, the phase margin of 30

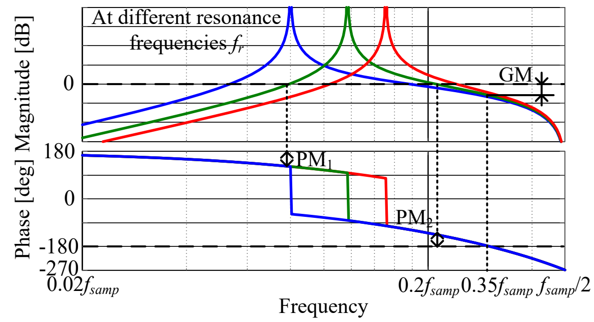

Fig. 5. Definition of gain and phase margins of inner loop at different resonance frequencies.

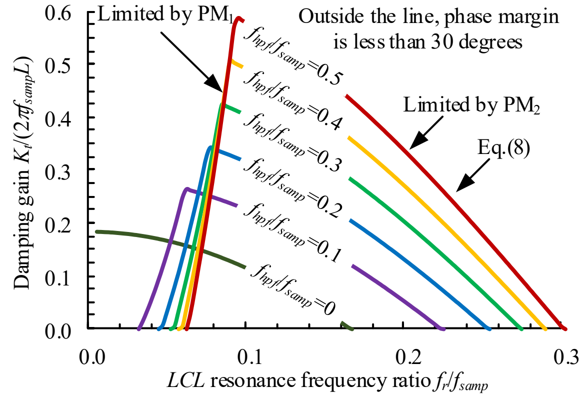

Fig. 6. Relationship between cutoff frequency and damping gain to achieve a phase margin of 30 degrees.

degrees or more is not achieved when the λ is 0.5. Furthermore, in the worst case, which is $0.35f_{samp}$ or more, the inner loop might be unstable. It is a limit of the HPF active damping method.

Fig. 6 depicts the relationship between the cutoff frequency of HPF and the LCL resonance frequency considering the active damping gain to achieve PM = 30 degrees. As shown in Fig. 6, The range of the LCL resonance frequency is limited to $0.3f_{samp}$ when the cutoff frequency of HPF is set to $0.5f_{samp}$. As shown in Fig. 6, the stable range is decreased as compared with the stable range in Fig. 6 by considering the phase margin. The inside of these triangles in Fig. 6 are the stable region of the operation with the active damping. Note that the increasing part of the triangle is decided from PM_1, and the decreasing part of the triangle is decided from PM_2. As a design guide, the active damping controller parameters design to satisfy the phase margin PM_2 at the maximum LCL resonance frequency, which is the stiff grid. The equation by polynomial curve fitting in Fig. 6 is expressed by

$$y \cong a_2x^2 + a_1x + a_0$$
$$\begin{cases} a_2 = -2278.3w^6 + 4064.8w^5 - 2905.54w^4 \\ \quad\quad +1075.1w^3 - 225.49w^2 + 24.62w - 6.3423 \\ a_1 = -0.77674w - 0.045246 \\ a_0 = 0.98265w + 0.19033 \end{cases} \tag{8}$$

where y is $K_t/(2\pi f_{samp}L)$, x is f_r/f_{samp}, and w is f_{hpf}/f_{samp}. Therefore, the active damping gain is determined by the LCL resonance frequency and the cutoff frequency of HPF. Next, the cutoff frequency of HPF is determined to maximize the current controller gain based on the root locus. The open-loop transfer function of the discrete grid current feedback control system in Fig. 3 is expressed by

$$G_{op}[z]=\frac{G_C[z]G_{v_O\to i_g}[z,m]}{1+G_{AD}[z]G_{v_O\to i_C}[z,m]} \tag{9}$$

Fig. 7 depicts the pole trajectory of the closed-loop transfer function of the discrete grid current feedback control system at the stiff grid, i.e. the grid inductance of 0 mH. The cutoff frequency of HPF is swept from 0 to the Nyquist frequency. The current controller is only proportional gain K_p for simplicity. As shown in Fig. 7, the poles move into the unit circle, i.e. the grid current feedback control system becomes stable by increasing the cutoff frequency of HPF. The instability at the low cutoff frequency of HPF is insufficient damping due to the destabilization of the inner loop. On the other hand, the instability at the high cutoff frequency of HPF is due to the decrease in the outer loop gain margin. As shown in Fig. 7, the cutoff frequency of HPF is determined to maximize the current controller gain. If the current controller gain is small, the control performance decrease. Thus, maximizing the current controller gain is an important factor.

Fig. 8 depicts the gain range of the current controller where the current control system is stabilized by the cutoff frequency of HPF. As shown in Fig. 8, there is the cutoff frequency of HPF to maximize the current controller gain by the *LCL* resonance frequency. The current controller gain with the HPF active damping method is lower than that with the proportional active damping method, which is clearly a weakness of the HPF active damping method. The maximum K_p at the resonance frequency when the cutoff frequency of HPF to maximize the current controller gain is selected is given by the polynomial curve fitting as follows

$$\begin{aligned}y\cong\ &437398x^8-640416x^7+378886x^6\\&-116724x^5+19892x^4-1805.3x^3\\&+75.692x^2-1.7x+0.195452\end{aligned} \tag{10}$$

where y is $K_p/(2\pi f_{samp}(L+L_f))$, x is f_r/f_{samp}.

Fig. 9 depicts the characteristics of the *LCL* resonance frequency and the cutoff frequency of HPF to achieve the maximum current controller gain. Note that the maximum current controller gain means the stability limit. The equation by polynomial curve fitting in Fig. 9 is expressed as follows

$$y\cong\begin{cases}0 & for\left(f_r/f_{samp}\le 0.1\right)\\ 134.08x^3-48.747x^2+6.9042x-0.3342 & \\ & for\left(0.1<f_r/f_{samp}<0.26\right)\\ 0.5 & for\left(0.26\le f_r/f_{samp}\right)\end{cases} \tag{11}$$

where y is f_{hpf}/f_{samp}, x is f_r/f_{samp}. The proportional active damping method is effective when the *LCL* resonance frequency is less than $0.1f_{smap}$. Otherwise, the HPF active damping method is effective and the cutoff frequency of HPF is set to $0.5f_{samp}$ when the *LCL* resonance frequency is $0.26f_{samp}$ or more.

III. Design of Multiple Object

Fig. 10 describes the *LCL* filter and the controller design procedure base on the *LCL* resonance frequency. The *LCL* filter and the controller design starts with the initialization of the following parameters; the nominal power P_n, the dc-link voltage V_{dc}, the grid voltage V_g, the grid frequency f_g, the switching frequency f_{sw}, the sampling frequency f_{samp}, the fraction of sampling period m, the number of output voltage levels N. First, the desired *LCL* resonance frequency at the stiff grid is selected based on the ratio to the sampling frequency. The inverter side inductance is determined by the current ripple ratio α(=

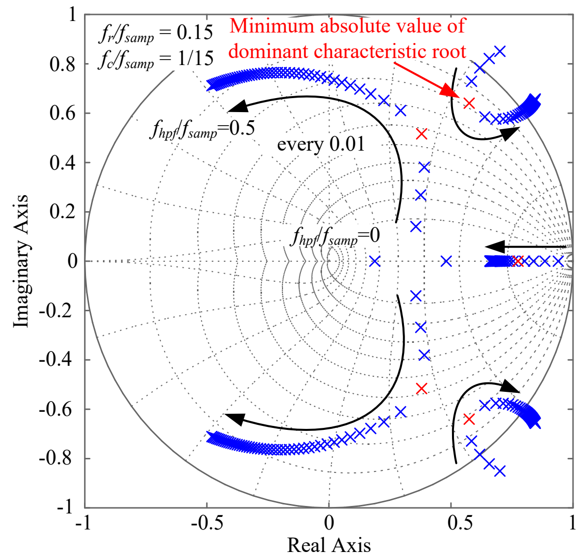

Fig. 7. Root locus of grid current feedback system when cutoff frequency of HPF is swept.

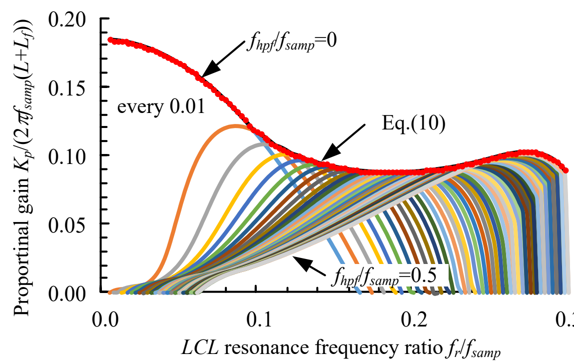

Fig. 8. Gain range of current controller where current control system is stabilized by HPF cutoff frequency.

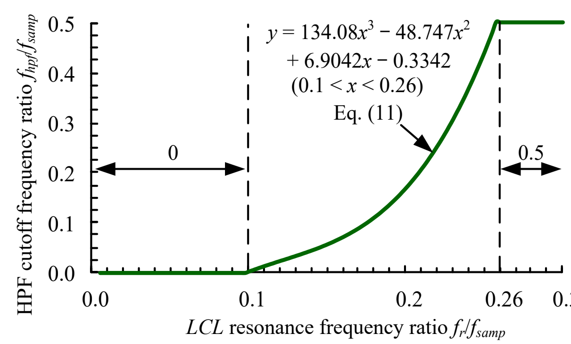

Fig. 9. Relationship between resonant frequency and cutoff frequency of HPF to maximize gain of grid current feedback system.

$\Delta i_L/I_{L\mathrm{rms}}$). Next, the relationship between the LCL resonance frequency and minimum k (= L_f/L) satisfying design requirements is calculated considering the five design requirements as follows: the reactive power restriction and harmonic suppression, the crossover frequency restriction at weak grid, the phase margin restriction at weak grid, and the power factor at stiff grid. Then, the minimum k and maximum f_r that satisfy these conditions are determined by drawing in the figure. Finally, the cutoff frequency of HPF is determined by the LCL resonance frequency at the stiff grid. The active damping gain is determined by the LCL resonance frequency and the cutoff frequency of HPF. The important definition of each parameter in this design is expressed as follows, respectively

$$Z_b = \frac{V_g^{\,2}}{P_n} \tag{12}$$,

$$\%Z_L = \frac{2\pi f_g L}{Z_b} \tag{13}$$,

$$C_f = \%Y_{C_f} C_b = \%Y_{C_f} \frac{1}{2\pi f_g Z_b} \qquad (\%Y_{C_f} \le 5\%) \tag{14}$$,

$$L_f = kL = k\%Z_L \frac{Z_b}{2\pi f_g} \qquad (0 < k \le 1) \tag{15}$$,

$$f_r = f_g \sqrt{\frac{\%Z_L(1+k) + \%Z_{L_g}}{\%Y_{C_f}\,\%Z_L\left(k\%Z_L + \%Z_{L_g}\right)}} \tag{16}$$,

$$f_{r\_\max}\Big|_{\%Z_{L_g}=0} = f_g \sqrt{\frac{1+k}{k\%Y_{C_f}\,\%Z_L}} \tag{17}$$,

$$f_{r\_\min}\Big|_{\%Z_{L_g}=\infty} = f_g \sqrt{\frac{1}{\%Y_{C_f}\,\%Z_L}} \tag{18}$$,

where Z_b is the base impedance, $\%Z_L$ is the inverter-side percentage impedance, C_b is the base capacitance, $\%Y_{Cf}$ is the percentage capacitance, k is the ratio of the inverter side inductance and the grid-side inductance, $\%Z_{Lg}$ is the grid impedance, f_{r_max} is the maximum LCL resonance frequency as stiff grid, and f_{r_min} is the minimum LCL resonance frequency as weak grid. Generally, worst case of grid impedance $\%Z_{Lg}$ is 10% [18]. Note that the filter capacitor is limited by the decrease of the power factor at the rated power (generally less than 5%) [19].

In this paper, the grid-side feedback current control applies a PI controller. Note that the controller parameter design without the filter capacitor voltage feedforward and with employed the low-inverter-side inductance is required to be more carefully determined for the system with the PI controller than for the system with a PR controller. The discretized transfer function of the PI controller is expressed by

$$G_C[z] = \frac{K_p}{T_i}\,\frac{\left(T_i + T_{samp}\right)z - T_i}{z-1} \tag{19}$$

where K_p is the proportional gain, and T_i is the integral period. Basically, The LCL resonance makes no phase contribution until the resonance frequency is actually reached [16], [17]. In this case, the phase is approximated by the ideal L filter-based system, which transfer function is written as

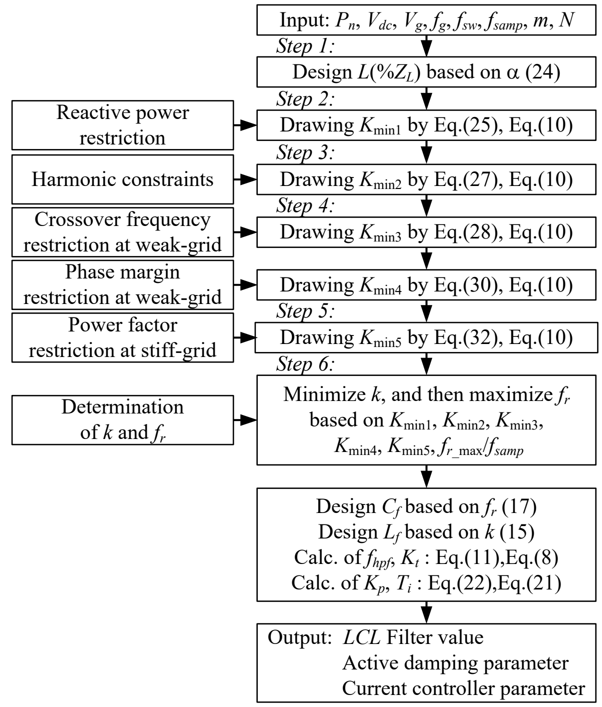

Fig. 10 Design flowchart of LCL filter and controller parameters

$$G_{v_O \to i_g}[z,m] \cong \frac{\omega_g T_{samp}\left[m(z-1)+1\right]}{Z_b\left(\%Z_L(1+k) + \%Z_{L_g}\right)z(z-1)} \tag{20}$$.

The integral period and the proportional gain are calculated from the crossover frequency f_c and the phase margin PM based on (19) and (20), which the integral period and the proportional gain are expressed by, respectively

$$T_i = \frac{T_{samp}}{2}\left[\frac{\tan\left(PM + \omega_c T_{samp}\right)}{\tan 0.5\omega_c T_{samp}} - 1\right] \tag{21}$$,

$$K_p = T_i \frac{\%Z_L(1+k)Z_b}{\omega_g}\,\frac{\left(\dfrac{2}{T_{samp}}\tan 0.5\omega_c T_{samp}\right)^2}{\sqrt{1+\tan^2\left(PM + \omega_c T_{samp}\right)}} \tag{22}$$.

Note that the current controller design is applied by assuming $L_g = 0$. According to (21), the crossover frequency is limited as follows

$$\frac{f_c}{f_{samp}} < \frac{\pi/2 - PM}{2\pi} \tag{23}$$.

Thus, the maximum crossover frequency is limited below (10) and (23). Within these ranges, the PI controller parameters to achieve the desired power factor PF, the phase margin PM_{weak}, and the crossover frequency f_{c_weak} at weak grid are determined.

Step 1: Design inverter side inductance L ($\%Z_L$)

Based on the current ripple ratio α (= $\Delta i_L/I_{L\mathrm{rms}}$) of the inverter-side inductor, the impedance of the inverter-side inductor is expressed by

$$\%Z_L = \frac{2\pi f_g V_{dc}}{4(N-1)^2 f_{sw} V_g \alpha} \tag{24}$$.

Step 2: Derivation of K_{min1} satisfying reactive power restriction

The relationship between the *LCL* resonance frequency and *k* considering the reactive power restriction is expressed as follows with (17),

$$K_{\min 1}=\left[\%Z_L\left(\frac{f_{samp}}{f_g}\frac{f_r}{f_{samp}}\right)^2\%Y_{C_f\max}-1\right]^{-1} \quad (25).$$

Step 3: Derivation of K_{min2} satisfying harmonic constraints

Based on the regulation of IEEE standard 1547, the relationship between percentage capacitance and the ratio of the inverter-side inductance and the grid-side filter inductance for satisfying current harmonics suppression is expressed by,

$$k\%Y_{C_f}>\frac{1}{\%Z_L}\left(\frac{f_g}{(N-1)f_{sw}}\right)^2\left(1+\frac{1}{0.3\%}\frac{4}{\pi^2}\alpha\right) \quad (26).$$

Moreover, the relationship between the *LCL* resonance frequency and *k* considering the harmonic suppression regulation is expressed as follows with (17) and (26),

$$K_{\min 2}=\left(\frac{f_r}{f_{samp}}\frac{f_{samp}}{(N-1)f_{sw}}\right)^2\left(1+\frac{1}{0.3\%}\frac{4}{\pi^2}\alpha\right)-1 \quad (27).$$

Step 4: Derivation of K_{min3} and K_{min4} satisfying crossover frequency and phase margin at weak grid

The relationship between the *LCL* resonance frequency and *k* considering the crossover frequency and phase margin at weak gird is expressed as follows with (10) and (19)- (22),

$$K_{\min 3}=\frac{\%Z_{L_g}}{\%Z_L}\frac{1}{F_1-1}-1 \quad (28),$$

$$F_1=\frac{\tan^2 0.5\omega_c T_{samp}}{\tan^2 0.5\omega_{c\_weak}T_{samp}}\cdot\sqrt{\frac{1+\dfrac{\tan^2 0.5\omega_{c\_weak}T_{samp}}{\tan^2 0.5\omega_c T_{samp}}\tan^2\left(PM+\omega_c T_{samp}\right)}{1+\tan^2\left(PM+\omega_c T_{samp}\right)}} \quad (29),$$

$$K_{\min 4}=\frac{\%Z_{L_g}}{\%Z_L}\frac{1}{F_2-1}-1 \quad (30),$$

$$F_2=\frac{\tan^2\left(PM+\omega_c T_{samp}\right)}{\tan^2\left(PM_{weak}+\omega_{c\_weak}T_{samp}\right)}\cdot\sqrt{\frac{1+\tan^2\left(PM_{weak}+\omega_{c\_weak}T_{samp}\right)}{1+\tan^2\left(PM+\omega_c T_{samp}\right)}} \quad (31).$$

Step 5: Derivation of K_{min5} satisfying power factor at stiff grid

The power factor is derived by the continuous system model, assuming the influence of the computation delay on the grid frequency is small enough. The relationship between the *LCL* resonance frequency and *k* considering the power factor at stiff gird is expressed by

TABLE I System Parameters

Circuit Parameter		
V_{DC}	DC-link Voltage	350 V
V_g	Grid Voltage	200 V_{rms}
P_n	Nominal Power	1 kW
f_g	Grid Frequency	50 Hz
Z_b	Base Impedance	40 Ω
C_b	Base Capacitance	79.6 μF
Switching Device (SiC-MOSFET)		SCT3030AL
f_{sw}	Switching Frequency	100 kHz
α	Current Ripple Ratio	31.25%
L	Inductor ($\%Z_L$ = 0.44%)	560 μH
C_f	Filter Capacitor ($\%Y_{Cf}$ = 1.25%)	1 μF
L_f	Filter Inductor (k = 0.42)	235 μH
$f_{r\ stiff}$	*LCL* Resonance Frequency	12.5 kHz
Controller Parameter		
f_{samp}	Sampling Frequency	50 kHz
m	Fraction of sampling period	0.5
T_d	Dead time	200 ns
f_c	Crossover Frequency	3.2 kHz
PM	Phase Margin	45 deg
K_p	Proportional Gain	13.8 Ω
T_i	Integral Period	111.7 μs
K_t	Active Damping Gain	25.9 Ω
f_{hpf}	Cutoff Frequency of HPF	22 kHz

$$K_{\min 5}=\frac{AV_g^2}{\%Z_L Z_b P_{out}\left[\tan\left(\cos^{-1}PF+\tan^{-1}\dfrac{B}{1-A}\right)-B\right]}-1$$

$$\begin{cases} A=\left(\dfrac{\omega_g T_{samp}}{2}\right)^2\dfrac{\sqrt{1+\tan^2\left(PM+\omega_c T_{samp}\right)}}{\tan^2 0.5\omega_c T_{samp}} \\ B=\dfrac{\omega_g T_{samp}}{2}\left[\dfrac{\tan\left(PM+\omega_c T_{samp}\right)}{\tan 0.5\omega_c T_{samp}}-1\right] \end{cases} \quad (32).$$

Step 6: Select k and f_r and *Design C_f, L_f, f_{hpf}, K_t, T_i, and K_p*

The recommended values of k and f_r within the range satisfying the requirements are desired to be small k and then large f_r in order to minimize the *LCL* filter. Based on k and f_r selected, each parameter is designed as follows; C_f is designed by (17), L_f is designed by (15), f_{hpf} is designed by (11), K_t is designed by (8), T_i is designed by (21), and K_p is designed by (22).

IV. DESIGN EXAMPLE

Table I shows the system parameters for the experiments. The robustness is examined with L_g varying by more than $\%Z_{Lg}$ = 10%, which corresponds to 12.7 mH.

According to the design flowchart in Fig. 10, first, substituting the current ripple ratio α = 31.25% into (19) and (13), $\%Z_L$ = 0.44 and L = 560 μH are calculated.

Fig. 11 depicts the relationship between f_r and k considering reactive power restriction in (25), current harmonics suppression regulation in (27), the crossover frequency restriction at weak gird in (28), the phase margin restriction at weak grid in (30), and the power factor restriction at stiff grid in (32). Finally, the *LCL* filter parameters and controller parameters are determined by considering the control performance, i.e. the power factor for stiff grid, the crossover frequency and the phase margin for weak

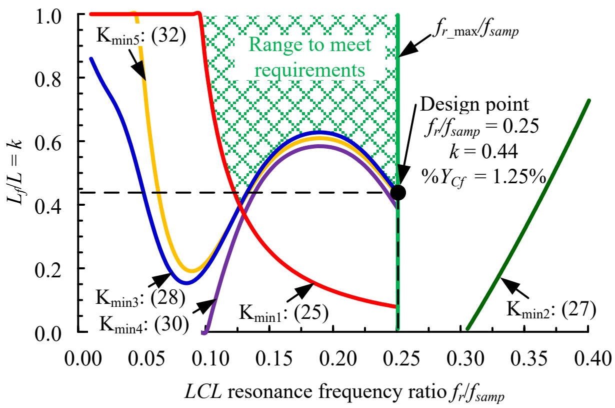

Fig. 11. Relationship between f_r and k considering current harmonics suppression regulation, resonance frequency, crossover frequency at weak-grid, phase margin at weak-grid and power factor at stiff-grid.

grid. As a result, f_c = 3.2 kHz, K_p = 13.8 Ω, T_i = 111.7 μs are decided from (25)-(32) when the condition is required as follows; PM = 45 degrees, PM_{weak} = 17 degrees, f_{c_weak} = 500 Hz, PF = 0.995.

Fig. 12 depicts the inner and outer loop characteristics of the controller. As shown in Fig. 12 (a), the stability margin of the inner loop is robust to the grid impedance variation. The phase margin of the inner loop at $\%Z_{Lg}$ = 0% is PM = 30 degrees according to the design strategy. The design values of the crossover frequency and the phase margin are 3.2 kHz and 45 degrees, although note that these actual values have errors due to the approximation of the circuit model as shown in Fig. 12 (b).

Fig. 13 depicts the pole trajectory of the current control system. As the grid impedance increases, the pole moves toward the boundary of the circle, i.e. the response of the system becomes poor. However, the system is stable even with grid impedance variation. Thus, the proposed design method enhances the system robustness to the grid impedance variation.

V. Experimental Results

Fig. 14 shows the experimental waveforms to verify the validity of the theoretical analysis, with the different grid impedances. As shown in Fig. 14 (a) and (b), the system stably operates without the resonant current. In other words, the good grid-tied operation is achieved regardless of the grid impedance. The grid current THD is maintained below 1.2% over the grid impedance range from 0% to 10%.

Fig. 15 shows the experimental waveforms to verify the validity of the theoretical analysis, with or without active damping. As shown in Fig. 15 (a), the system stably operates without resonant current when the active damping is enabled, whereas the system stably operates even without the active damping as shown in Fig.15 (b). The reason for the stable operation in Fig. 15 (b) is the nonlinearity of the discontinuous current mode is induced by the dead-time.

VI. Conclusion

This paper proposed the comprehensive design strategy for the LCL filter and the controller parameters of the active damped LCL filter system with the low inverter-side inductance in the grid-tied inverter.

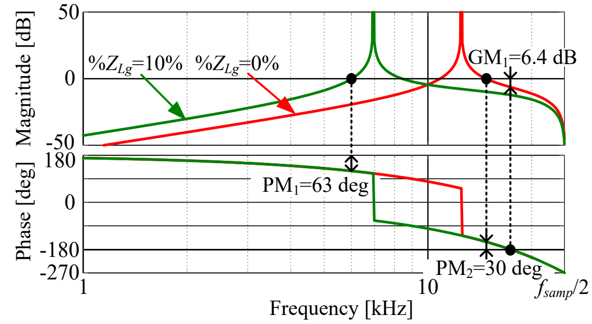

(a) Inner loop due to filter capacitor current feedback for active damping.

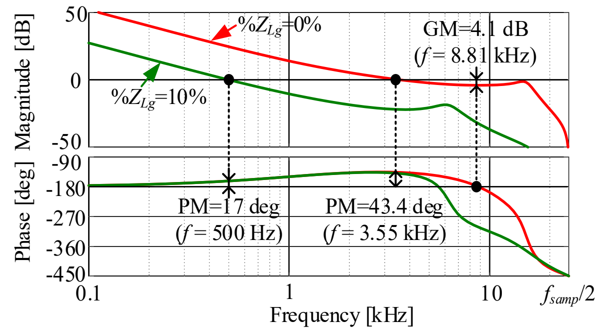

(b) Outer loop due to grid current feedback for current control.

Fig. 12. Inner and outer loop characteristics.

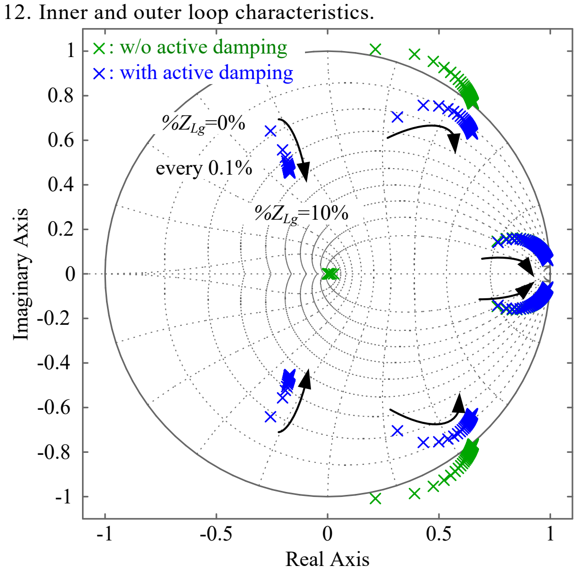

Fig. 13. Root locus of grid current feedback system when grid inductance is swept.

The influence of the active damping gain and the grid impedance on the stability of the active damped LCL filter in the single-phase grid-tied inverter was clarified. Then, the practical implementation solutions were discussed based on the proposed design procedure. The detailed design strategy was exhibited with the design procedure and the design example. The experimental results were provided to verify the effectiveness of the design strategy. The grid current THD is maintained below 1.2% over the grid impedance range from 0% to 10%.

References

[1] IEEE Application Guide for IEEE Std 1547(TM), IEEE Standard for Interconnecting Distributed Resources with Electric Power Systems," in *IEEE Std 1547.2-2008* , vol., no., pp.1-217, 15 April 2009

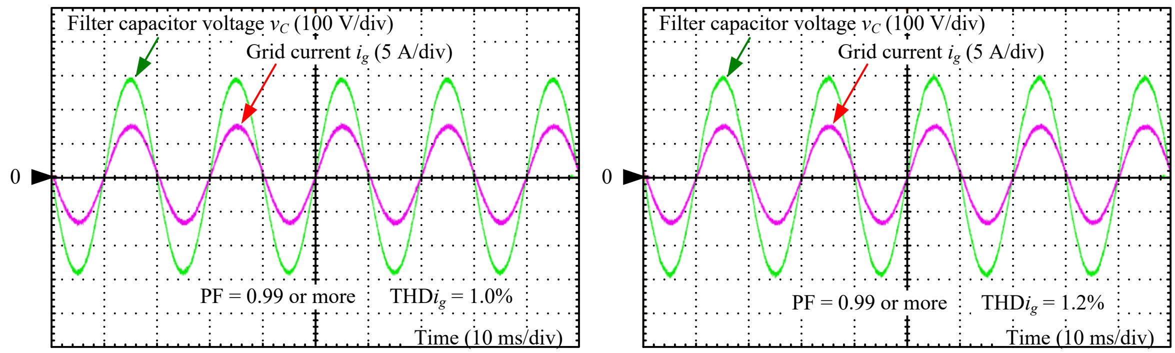

(a) Stiff grid at $\%Z_g = 0\%$ ($L_g = 0$ mH). (b) Weak grid at $\%Z_g = 10\%$ ($L_g = 12.7$ mH).

Fig. 14. Inverter operation waveforms with active damping.

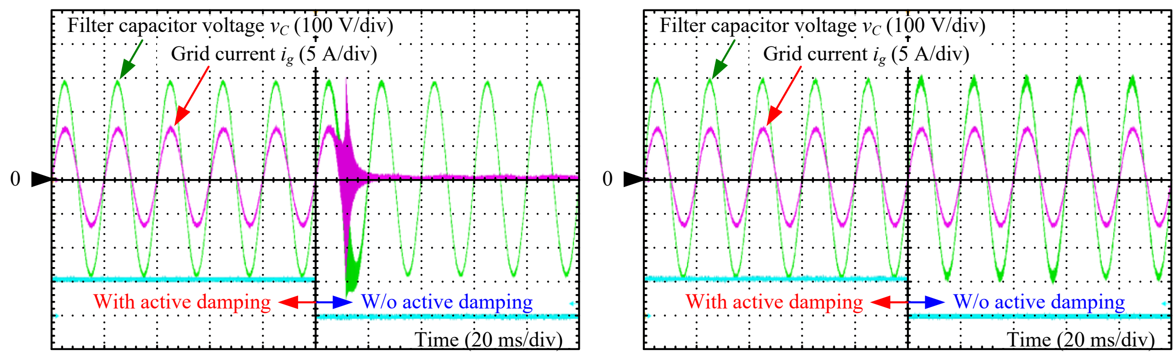

(a) Stiff grid at $\%Z_g = 0\%$ ($L_g = 0$ mH). (b) Weak grid at $\%Z_g = 10\%$ ($L_g = 12.7$ mH).

Fig. 15. Inverter operation waveforms when active damping is disabled from enabled.

[2] W. Wu, Y. He, T. Tang and F. Blaabjerg, "A New Design Method for the Passive Damped LCL and LLCL Filter-Based Single-Phase Grid-Tied Inverter," in *IEEE Transactions on Industrial Electronics*, vol. 60, no. 10, pp. 4339-4350, Oct. 2013.

[3] C.T. Lee, A. Kikuchi, and T. Ito,"An Auto-Tuning Damper for the Harmonic Resonance of Grid-Connected Converters,"IEEJ J. Industry Applications, vol. 8, no. 6, pp. 884–892, 2019.

[4] Tuomas Messo, Roni Luhtala, Aapo Aapro, and Tomi Roinila"Accurate Impedance Model of a Grid-Connected Inverter for Small-Signal Stability Assessment in High-Impedance Grids,"IEEJ J. Industry Applications, vol. 8, no. 3, pp. 488-496, 2019.

[5] M. Semasa, T. Kato, K. Inoue, "Simple and Effective Time Delay Compensation Method for Active Damping Control of Grid-Connected Inverter with an LCL Filter", in *IEEJ Journal of Industry Applications*,.vol. 7, no. 6, pp. 454-461, 2018

[6] P. Mattavelli, F. Polo, F. Dal Lago and S. Saggini, "Analysis of Control-Delay Reduction for the Improvement of UPS Voltage-Loop Bandwidth," in *IEEE Trans. on Ind. Electron.*, vol. 55, no. 8, pp. 2903-2911, Aug. 2008.

[7] D. Pan, X. Ruan, X. Wang, F. Blaabjerg, X. Wang and Q. Zhou, "A Highly Robust Single-Loop Current Control Scheme for Grid-Connected Inverter With an Improved LCCL Filter Configuration," in *IEEE Trans. on Power Electronics*, vol. 33, no. 10, pp. 8474-8487, Oct. 2018.

[8] S. G. Parker, B. P. McGrath and D. G. Holmes, "Regions of Active Damping Control for LCL Filters," in *IEEE Transactions on Industry Applications*, vol. 50, no. 1, pp. 424-432, Jan.-Feb. 2014.

[9] J. Wang, J. D. Yan, L. Jiang and J. Zou, "Delay-Dependent Stability of Single-Loop Controlled Grid-Connected Inverters with LCL Filters," in *IEEE Trans. on Power Electron.*, vol. 31, no. 1, pp. 743-757, Jan. 2016.

[10] C. Zou, B. Liu, S. Duan and R. Li, "Influence of Delay on System Stability and Delay Optimization of Grid-Connected Inverters With LCL Filter," in *IEEE Trans. on Ind. Inform.*, vol. 10, no. 3, pp. 1775-1784, Aug. 2014.

[11] X. Li, J. Fang, Y. Tang, X. Wu and Y. Geng, "Capacitor-Voltage Feedforward With Full Delay Compensation to Improve Weak Grids Adaptability of LCL-Filtered Grid-Connected Converters for Distributed Generation Systems," in *IEEE Transactions on Power Electronics*, vol. 33, no. 1, pp. 749-764, Jan. 2018.

[12] M. Lu, A. Al-Durra, S. M. Muyeen, S. Leng, P. C. Loh and F. Blaabjerg, "Benchmarking of Stability and Robustness Against Grid Impedance Variation for LCL -Filtered Grid-Interfacing Inverters," in *IEEE Trans. on Power Electronics*, vol. 33, no. 10, pp. 9033-9046, Oct. 2018.

[13] W. Yao, Y. Yang, Y. Xu, F. Blaabjerg, S. Liu and G. Wilson, "Phase Reshaping via All-Pass Filters for Robust LCL-Filter Active Damping," in *IEEE Transactions on Power Electronics*, vol. 35, no. 3, pp. 3114-3126, March 2020.

[14] D. Pan, X. Ruan, C. Bao, W. Li and X. Wang, "Capacitor-Current-Feedback Active Damping With Reduced Computation Delay for Improving Robustness of LCL-Type Grid-Connected Inverter," in *IEEE Trans. on Power Electronics*, vol. 29, no. 7, pp. 3414-3427, July 2014.

[15] X. Wang, F. Blaabjerg and P. C. Loh, "Virtual RC Damping of LCL-Filtered Voltage Source Converters With Extended Selective Harmonic Compensation," in *IEEE Transactions on Power Electronics*, vol. 30, no. 9, pp. 4726-4737, Sept. 2015.

[16] Y. He, X. Wang, X. Ruan, D. Pan, X. Xu and F. Liu, "Capacitor-Current Proportional-Integral Positive Feedback Active Damping for LCL-Type Grid-Connected Inverter to Achieve High Robustness Against Grid Impedance Variation," in *IEEE Transactions on Power Electronics*, vol. 34, no. 12, pp. 12423-12436, Dec. 2019.

[17] D. Pan, X. Ruan, C. Bao, W. Li and X. Wang, "Optimized Controller Design for *LCL*-Type Grid-Connected Inverter to Achieve High Robustness Against Grid-Impedance Variation," in *IEEE Transactions on Industrial Electronics*, vol. 62, no. 3, pp. 1537-1547, March 2015.

[18] M. Liserre, R. Teodorescu and F. Blaabjerg, "Stability of photovoltaic and wind turbine grid-connected inverters for a large set of grid impedance values," in *IEEE Transactions on Power Electronics*, vol. 21, no. 1, pp. 263-272, Jan. 2006.

[19] S. Jayalath and M. Hanif, "Generalized LCL-Filter Design Algorithm for Grid-Connected Voltage-Source Inverter," in *IEEE Transactions on Industrial Electronics*, vol. 64, no. 3, pp. 1905-1915, March 2017.